

Analysis of Heterogeneous Cardiac Pacemaker Network Models and Traveling Wave Dynamics

Cheng Ly^{a,*}, Seth H. Weinberg^{b,*}

^a*Department of Statistical Sciences & Operations Research, Virginia Commonwealth University*

^b*Department of Biomedical Engineering, Virginia Commonwealth University*

Abstract

The sinoatrial-node (SAN) is a complex heterogeneous network that generates a stable rhythm in healthy hearts, yet a general mechanistic explanation for when and how these networks remain stable is lacking. Although computational and theoretical analyses could elucidate this phenomena, such methods have rarely been used in realistic (large-dimensional) gap-junction coupled heterogeneous pacemaker cell models. In this study, we adapt a recent model of pacemaker cells (Severi et al., 2012), incorporating biophysical representations of ion channel and intracellular calcium dynamics, to capture physiological features of a heterogeneous population of pacemaker cells; in particular “center” and “peripheral” cells with distinct intrinsic frequencies and action potential morphology. Large-scale simulations of the SAN tissue, represented by heterogeneous networks of pacemaker cells, exhibit a rich repertoire of behaviors, including complete synchrony, traveling waves of activity originating from periphery to center, and transient traveling waves originating from the center. We use phase reduction methods that do not require fully simulating the large-scale model to capture these observations. Moreover, the phase reduced models accurately predicts key properties of the tissue electrical dynamics, including wave frequencies when synchronization occurs, and wave propagation direction in a variety of network models. Further, with the reduced phase models, we analyze the relationship between cell distributions and coupling strengths and the resulting transient dynamics. Thus, we demonstrate that phase reduced oscillator models applied to realistic pacemaker networks provide novel insights into the spatial-temporal dynamics of cardiac pacemaker activity.

Keywords:

Sinoatrial-node, Traveling Waves, Heterogeneous pacemaker cells, Phase Reduction, Phase Oscillators

1. Introduction

The sinoatrial node (SAN) is the region of the heart responsible for generating the electrical rhythm. Although isolating individual cardiac pacemaker cells in the SAN to experimentally measure electrophysiological properties is feasible (Honjo et al., 1996; Kodama et al., 1997), a

*Corresponding authors

Email addresses: cly@vcu.edu (Cheng Ly), shweinberg@vcu.edu (Seth H. Weinberg)

URL: www.shweinberglab.com (Seth H. Weinberg)

detailed understanding of the dynamics of intact coupled networks of cardiac cells (i.e., tissue) is difficult for several reasons. The SAN structure is highly complex at both the cellular and network levels, with heterogeneous gap junctional coupling. Only a few studies have investigated SAN function experimentally (Fedorov et al., 2009; Efimov et al., 2010; Fedorov et al., 2010, 2012; Glukhov et al., 2013; Li et al., 2015; Csepe et al., 2016; Li et al., 2017). However, the mechanisms of how regular rhythms are generated in this complex cellular network are still not well understood. Computational modeling can play a valuable role in understanding the dynamics of healthy and diseased cardiac rhythms (Greer-Short et al., 2017; Phadumdeo and Weinberg, 2018; Arevalo et al., 2016), yet there have only been a few computational studies of the full SAN tissue (e.g., see Oren and Clancy (2010); Severi et al. (2012); Zhang et al. (2000); Wilders (2007)).

There is some uncertainty as to the degree of cellular heterogeneity within the cell population comprising the SAN tissue. Structural studies have described a “central” SAN region of smaller cells, with a transition to larger “peripheral” SAN cells (Bouman and Jongsma, 1986), with distinct action potential and calcium handling properties distinguishing these cell types (Honjo et al., 1996; Kodama et al., 1997). However, other studies have not found distinct isolated SAN cell electrical and calcium properties based on cell size (Michaels et al., 1987; Verheijck et al., 1998). In this study, we will investigate electrical properties in the SAN tissue, considering these two different approaches: SAN tissue comprised of (1) a homogeneous population of either all “center” cells or all “peripheral” cells (described further below); or (2) a heterogeneous population that transitions from center to peripheral cells.

While realistic large-scale SAN network models can yield insightful simulations, these systems are typically too complicated for detailed mechanistic descriptions of phenomena; a mathematical framework could aid this endeavor. To our knowledge, all computational studies of SAN tissue (Oren and Clancy, 2010; Severi et al., 2012; Zhang et al., 2000; Wilders, 2007) rely on large-scale tissue-scale simulations, without mechanistic mathematical analysis describing the critical properties that regulate cardiac electrical rhythms.

In this study, we apply mathematical methods for studying coupled heterogeneous oscillators (pacemaker cells) to analyze a novel minimal model of SAN tissue electrical activity. Our coupled oscillator model is developed from the periodic dynamics of a recent multi-compartment biophysical pacemaker model from Severi et al. (2012), with realistic calcium dynamics and ionic currents. Following prior work (Zhang et al., 2000; Kurata et al., 2002; Oren and Clancy, 2010), cellular heterogeneity attributes (i.e., differences between center and peripheral cells) in uncoupled cardiac pacemaker cells are represented by varying model cell size and ionic conductances. We then apply the theory of weakly coupled phase oscillators (Kopell and Ermentrout, 1986; Ermentrout, 1992) to formulate a reduced phase model and formulate a 1D “chain” of coupled phase oscillators, minimally representing the fully coupled SAN tissue in a manner that does not require simulating the full network.

We compare this reduced model with a biophysically detailed SAN tissue model with hundreds of cells, coupled via gap junctions. Computationally expensive simulations of several coupled SAN network models varying from homogeneous to heterogeneous cell populations results in a variety of spatio-temporal dynamics, including: persistent synchrony, persistent traveling waves that originates in the periphery, transient travel waves the originate in the center, etc. Our formulation of a 1D chain of phase oscillators captures the persistent wave frequency, synchronization, and wave propagation direction in a variety of large-scale SAN network models. Furthermore, this mathematical framework can predict the existence and stability of steady-state traveling waves and characterize the duration of transient activity before settling to a persistent

state. We demonstrate that this phase reduction method can qualitatively and, in some cases, quantitatively reproduce electrical properties of biophysically realistic and heterogeneous coupled SAN tissue.

2. Methods

Detailed Biophysical Pacemaker Cell Models

The SAN isolated cell and tissue models are based on the recent model from Severi et al. (2012), with the membrane potential for cell j (v_j) governed by the following current-balance equation,

$$C_j \frac{dv_j}{dt} = -I_{Na} - I_f - I_{to} - I_{Ca,L} - I_{Ca,T} - I_{Kr} - I_{Ks} - I_{Na,K} - I_{Na,Ca} - g_{gap} \sum_k (v_j - v_k), \quad (1)$$

where C_j is membrane capacitance and which incorporates biophysical descriptions of ionic currents (see Table 1 for names of currents), a detailed model of calcium handling including sarcoplasmic reticulum (network and junctional), and ionic current pumps and exchangers. There are 31 state variables for *each* pacemaker cell; see Appendix A for further details. The last term represents local coupling via gap junctions, $g_{gap} \sum_k (v_j - v_k)$, between cell j and cell k . Note that gap junctional conductance g_{gap} is only non-zero if cells j and k are coupled and further depend on distance from the tissue center in the heterogeneous coupling schemes considered.

For center cells, we use the same parameters as Severi et al. (2012) to match the reported action potential characteristics described in Zhang et al. (2000); Kodama et al. (1997); Oren and Clancy (2010). For the other types of pacemaker cells (i.e., transitioning from center to peripheral cells), we vary the following 12 parameters: cell capacitance, cell length, cell radius, and the maximum conductance of the funny currents, L-type and T-type calcium currents, slow and rapid delayed rectifier potassium currents, sodium current, sodium-potassium pump, and sodium-calcium exchanger. Parameter values for center and peripheral cells (Table 2) are based on values reported in Oren and Clancy (2010), and scale factors in Zhang et al. (2000).

Table 1: Definition of currents in Eq (1).

Equation	Name
I_{Na}	Sodium current
I_f	Funny current
I_{to}	Transient outward potassium current
$I_{Ca,L}$	L-type calcium current
$I_{Ca,T}$	T-type calcium current
I_{Kr}	Rapid delayed rectifier K ⁺ current
I_{Ks}	Slow delayed rectifier K ⁺ current
$I_{Na,K}$	Sodium-Potassium pump
$I_{Na,Ca}$	Sodium-calcium exchanger

Phase Reduced Model

To mathematically analyze the persistent (or steady-state traveling wave) behavior of the coupled pacemaker cells, we employ phase reduction methods, in which the dynamics of high dimensional systems are approximated with a simple scalar periodic variable. These methods have been successfully applied to many areas of science (Winfree, 1967), including chemical oscillations (Kuramoto, 2012), synchronization of fireflies (Mirollo and Strogatz, 1990), circadian rhythms (Winfree, 1970; Zeitzner et al., 2000), and cellular networks (Ermentrout and Terman, 2010; Schultheiss et al., 2011; Ly and Ermentrout, 2010), to name a few. We briefly describe the general approach here (see Chapter 9 of Ermentrout and Terman (2010)). Consider a large dimensional model $X_j \in \mathbb{R}^n$ coupled to $X_k \in \mathbb{R}^n$ of the form:

$$\frac{dX_j}{dt} = F(X_j) + \varepsilon G(X_j, X_k). \quad (2)$$

When there is an asymptotically stable limit cycle $X_0(t)$ with period T_j , for the uncoupled case $\varepsilon = 0$, we map values near the limit cycle to the unit circle via a function $\phi(X_j) := \Theta_j \in [0, T_j)$, to derive the following:

$$\frac{d\Theta_j}{dt} = 1 + \nabla_X \phi(X_j) \cdot \varepsilon G(X_j, X_k). \quad (3)$$

Since other cells X_k only directly effect the voltage variable, all components of $\nabla_X \phi(X_j) \cdot \varepsilon G(X_j, X_k)$ are 0 except the voltage component. For small ε , we approximate $\nabla_X \phi(X_j(\Theta_j)) \approx \nabla_X \phi(X_0(\Theta_j))$; the voltage component of this is the *phase-resetting curve* (**PRC**), which we denote by $\Delta_j(\Theta_j)$. Next, the method of averaging is applied to approximate the second term of Eq (2) with the function:

$$H_{j,k}(\Theta_k - \Theta_j) := \frac{1}{T_j} \int_0^{T_j} \Delta_j(t) G(X_j(t), X_k(t + \Theta_k - \Theta_j)) dt, \quad (4)$$

often called the interaction function (or H -function).

This phase reduction can be applied repeatedly for each of the different pacemakers, with a rescaling of time so that $\theta_j \in [0, 1)$ to arrive at the following phase network approximation:

$$\frac{d\theta_j}{dt} = \omega_j + \sum_k H_{j,k}(\theta_k - \theta_j) \quad (5)$$

Since we are interested in the direction of the traveling wave (if it exists) and the large SAN model is nearly radially symmetric in cell type, the phase model is further simplified to a 1-dimensional chain with “cut-ends”, with one end being the Center and the other being the Peripheral (see Fig. 3C). Furthermore, a relatively large number of cell types (9) are used to span the range from a prototypical center pacemaker to peripheral pacemaker, enabling us to assume a modest amount of heterogeneity among neighboring cells (see Fig. 1B). Since coupling is local via gap junctions, we approximate the interaction function (for $k = j - 1$ and $k = j + 1$ only):

$$H_{j,k}(x) \approx H_j(x) \quad (6)$$

where H_j is the interaction function of the j^{th} cell type with itself, which can be numerically computed with the program XPP (Ermentrout, 2002).

In order to systematically relate the 1D chain of phase oscillators to the large scale model, each of the cell types are grouped together, and an average conductance is calculated via:

$$\bar{g}_{gap,j} = \frac{1}{\# \text{ nonzero } g_{j,k}} \sum_k g_{j,k}.$$

4

Here, $g_{j,k}$ denotes the g_{gap} conductance (see Eq. (1)) between cell j and cell k (Fig. 2C left color-codes all 9 cell types by spatial location). This value of $\bar{g}_{gap,j}$ multiplies the corresponding pieces of the interaction functions (plotted in Fig. 3B):

$$H_{j,k} \approx \bar{g}_{gap,j} H_j. \quad (7)$$

We can use this phase reduction approach to determine the existence of traveling wave solutions. These solutions to equation (5) are of the form:

$$\theta_j(t) = \Omega t + \xi_j.$$

Quantifying Transient Times with Phase Models

If a stable persistent state exists for a given phase reduction and tissue network structure, we are also interested in the time required for the system to reach this persistent state, following a perturbation or from a given initial condition. We can calculate this transient time in the full SAN tissue model via simulation and compare with the reduced phase model framework. In the reduced phase model, consider a perturbation $\vec{\eta}(t)$ to a traveling wave solution $\Omega t + \vec{\xi}$

$$\theta_j(t) = \Omega t + \xi_j + \eta_j(t). \quad (8)$$

After substituting the above equation into Eq. (5) and assuming perturbations are small ($\eta_j = O(\varepsilon) \forall j$), the 1st order ε equation provides a linear approximation for the dynamics of $\eta_j(t)$:

$$\begin{aligned} \frac{d\eta_1}{dt} &= H'_{1,2}(\xi_2 - \xi_1)(\eta_2 - \eta_1) \\ \frac{d\eta_j}{dt} &= H'_{j,j-1}(\xi_{j-1} - \xi_j)(\eta_{j-1} - \eta_j) + H'_{j,j+1}(\xi_{j+1} - \xi_j)(\eta_{j+1} - \eta_j), \text{ for } j = 2, \dots, 8 \\ \frac{d\eta_9}{dt} &= H'_{9,8}(\xi_8 - \xi_9)(\eta_8 - \eta_9) \end{aligned} \quad (9)$$

This equation in matrix-vector form is:

$$\frac{d\vec{\eta}}{dt} = A\vec{\eta} \quad (10)$$

$$A := \begin{pmatrix} -H'_{1,2} & H'_{1,2} & 0 & \dots & \dots & \dots & 0 \\ \vdots & \vdots & \vdots & \vdots & \vdots & \vdots & \vdots \\ 0 & \dots 0 & H'_{j,j-1} & -H'_{j,j-1} - H'_{j,j+1} & H'_{j,j+1} & 0 \dots & 0 \\ \vdots & \vdots & \vdots & \vdots & \vdots & \vdots & \vdots \\ 0 & \dots & \dots & \dots & 0 & H'_{9,8} & -H'_{9,8} \end{pmatrix} \quad (11)$$

Each of the terms in the matrix abbreviated as: $H'_{j,k} := H'_{j,k}(\xi_k - \xi_j)$. When a traveling wave solution is stable, all but one of the eigenvalues of A have negative real part; there is a distinct zero eigenvalue $\lambda_0 = 0$ with eigenvector $\vec{1}$ that corresponds to a constant shift in the traveling wave solution¹.

¹A constant shift in all variables is a perturbation that does not decay, because the result is the same traveling wave solution.

Let the eigenvectors of A be $\vec{\psi}_j$ with eigenvalues λ_j : $A\vec{\psi}_j = \lambda_j\vec{\psi}_j$, then since A is symmetric, we take $\vec{\psi}_j$ to be an orthonormal set. With initial condition $\vec{\eta}_0$, the vector of perturbations is captured using an eigenvector expansion to solve for:

$$\frac{d\vec{\eta}}{dt} = A\vec{\eta}$$

to get:

$$\vec{\eta}(t) = \sum_{k \neq 0} (\vec{\psi}_k, \vec{\eta}_0) e^{\lambda_k t} \vec{\psi}_k.$$

The solution can be approximated by using only the largest real eigenvalue with an eigenvector expansion (excluding the 0 eigenvector):

$$\vec{\eta}(t) = (\vec{\psi}_1, \vec{\eta}_0) e^{\lambda_1 t} \vec{\psi}_1.$$

The operation (\vec{v}, \vec{w}) is the usual inner product. Fig S2 (S1Text.pdf) shows that this approximation is excellent for the networks and initial condition we consider.

3. Results

3.1. Large-scale Pacemaker Network

We first developed a population of physiologically realistic pacemaker cell models, using the Severi et al. (2012) model as the baseline center cell. This model includes a variety of gating variables, ionic currents, and cellular voltage and calcium dynamics. By altering 12 parameters, our modified model reproduces the wide-variety of intrinsic frequencies of cell-types and action potential morphology of pacemaker cells. While there is still much debate as the degree of heterogeneity within the SAN cell population, prior experimental work has shown that larger peripheral cells have faster intrinsic frequencies than smaller center cells, as well as other electrophysiological properties (Honjo et al., 1996; Kodama et al., 1997). The uncoupled frequency of peripheral cells is almost double ($\approx 1.8\times$ larger) than center cells (Fig. 1C inset). Additionally, action potential morphology is altered, as the voltage trace has a smaller minimum and larger maximum and overall shorter action potential duration in peripheral cells, compared with center cells (Fig. 1A), consistent with experimental recordings (Honjo et al., 1996; Kodama et al., 1997).

Next, we consider a model of the SAN tissue, represented by a network of 271 Severi pacemaker cells with coupling via nearest neighbor gap junctions (Fig. 2C). To mimic a radially symmetric architecture, the SAN tissue is represented by a 2D hexagonal grid of uniformly spaced cells, i.e., all connected cells have the same Euclidean distance apart. Simulation of the full biophysical representation of the SAN tissue are computationally expensive simulations, requiring several days to weeks to simulate 20 s of biological time for a single parameter set. These simulations presented with a variety of spatio-temporal dynamics that depend on coupling strength and cell distribution (heterogeneous or homogeneous).

To investigate the role of heterogeneity in the SAN tissue, we simulate a homogeneous network comprised of either all center (Fig. 2A) or all peripheral (Fig. 2B) cells, or a heterogeneous network with a transition from center to peripheral cell types (Fig. 2D). Experimental observations suggest that pacemaking originates in the center of the SAN tissue. Consistent with these conditions, for all three networks, we set the initial condition of all 31 state variables, such that

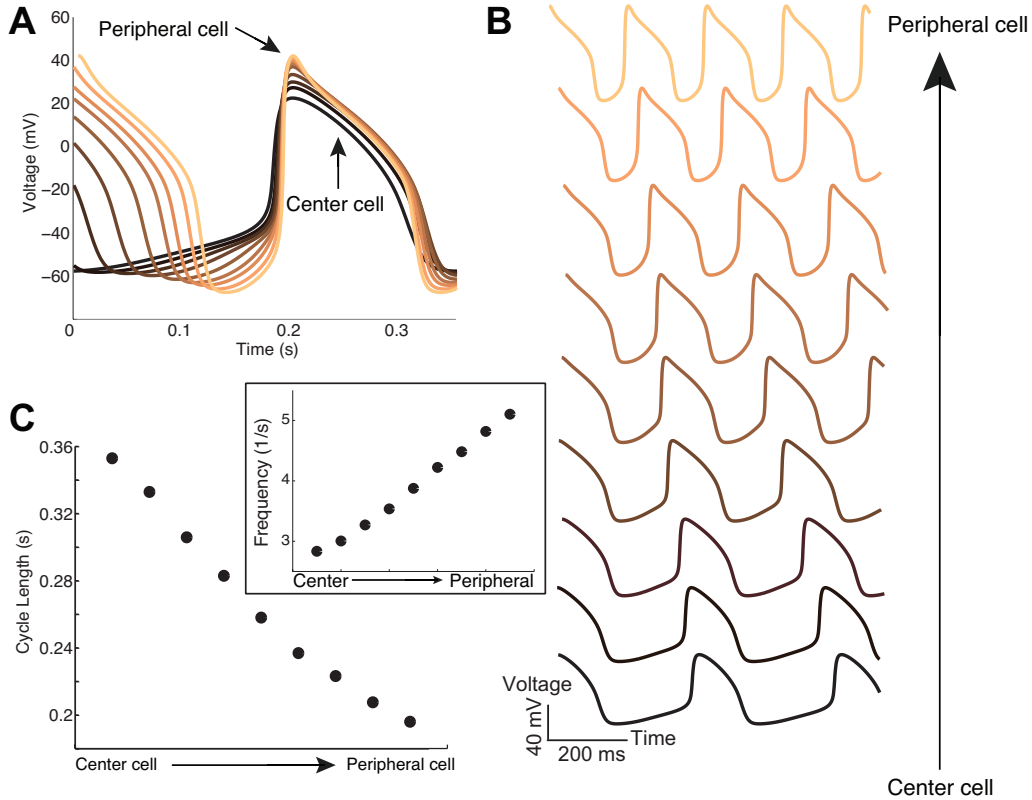


Figure 1: The full cardiac pacemaker model, showing all 9 heterogeneous cell types (uncoupled). **A**) The spike wave form for all 9 cells, shifted so the peaks are at the same time point to contrast waveforms. **B**) Voltage trace of the model over several beats for all 9 cell types. **C**) The cycle length (in seconds); the inset shows the frequency in 1/s.

center cells were “closer” to spiking and peripheral cells were “further” from spiking, in a gradual monotonic way (Fig. 2C right). This resulted in an initial but transient traveling wave that originated in the center for all three networks. Closer inspection of the voltage traces reveals that the transient dynamics have different durations; in particular, the transient persist longest in the homogeneous peripheral cell network, followed by the homogeneous center cell network, with the heterogeneous network having the shortest transient before settling to the steady-state wave solution. Interestingly, in both homogeneous cases, after an initial transient time period, electrical activity of all of SAN cells became highly synchronized. However, in the heterogeneous SAN tissue (Fig. 2C left), a brief transient period is followed by a stable traveling wave, originating in the periphery (Fig. 2D), consistent with findings by Oren and Clancy (2010). Note that the coupling strengths are the same for all connected cells and in all three networks ($g_{gap} = 0.25$ nS). Among other network attributes, transient times depend on initial conditions; here we chose the same qualitative initial condition that did not correspond to the steady-state traveling wave for any of the networks.

We did not exhaustively vary the coupling strengths g_{gap} in each network, because of com-

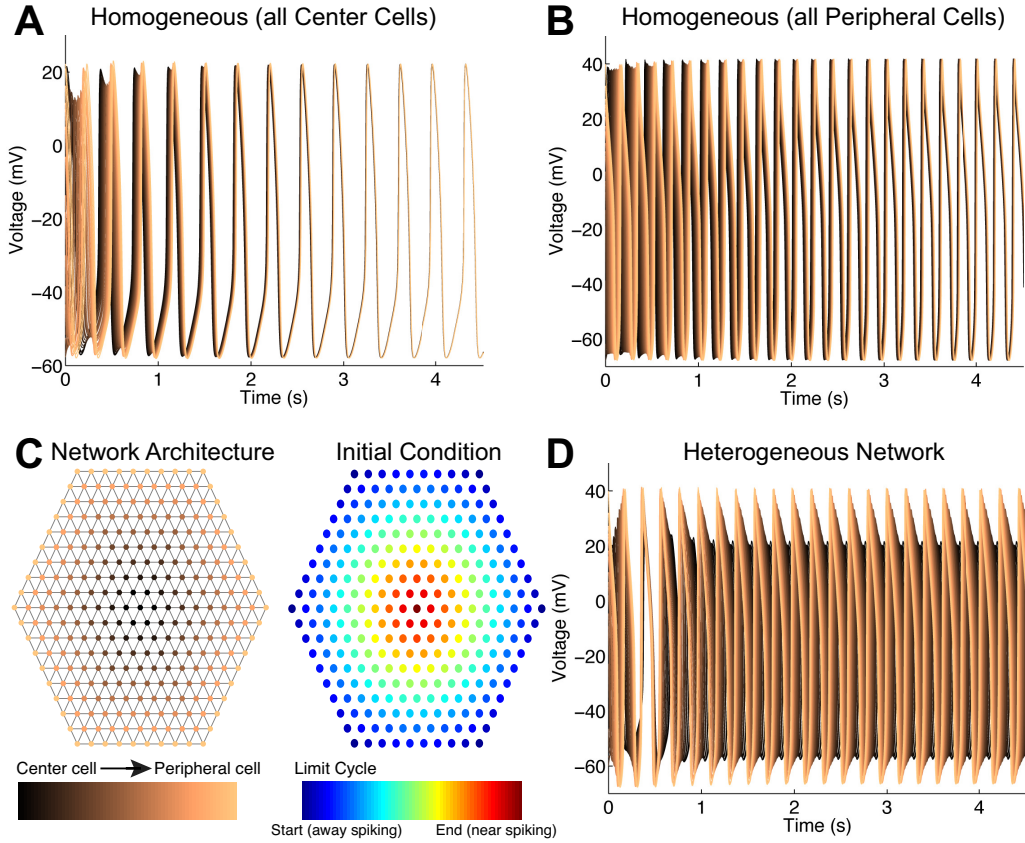


Figure 2: Simulation results of the full pacemaker model. The color-coding schemes in **A** and **B** do **not** represent intrinsically different cell types, but chosen to show spatial location. **A**) With identical cells (all center): after an initial transient of center-to-peripheral traveling wave, the system settles to complete synchrony. **B**) With identical cells (all peripheral), the transient center-to-peripheral wave lasts longer and has larger frequency than the center cells in **A**, but eventually settles to complete synchrony. **C**) Left) the network architecture is nearest neighbor coupling (gray lines connecting dots) used for all networks, the color coding indicates different cell types in the heterogeneous network used in **D**. There are 271 total pacemaker cells on a hexagonal grid with all connected cells equidistant apart. **C**) Right) the same initial condition for all networks where cells near the center are closer to spiking, and peripheral cells are gradually further away from spiking; this sets the network to transiently have traveling waves originating in the center. **D**) In a completely heterogeneous network, the transient (center-to-peripheral wave) is very brief, after which the system settles to a persistent traveling wave solution that originates in the periphery and ends in the center. In all panels, coupling strength was constant $g_{gap} = 0.25$ nS.

putational resources, but we did simulate each network with several sets of gap junction values. As coupling strength increases in a given network, the transient times generally decrease, as one might intuitively expect due to stronger interactions between cells (see Fig. 7 for the same networks as Fig. 2 but with larger g_{gap}). Although this is only apparent by inspection, we will show this is theoretically true in the next section with the reduced phase model theory.

Ultrastructure studies of the SAN tissue suggest that there may be an increase in gap junctional density from the center to the periphery (Masson-Pévet et al., 1979; Bleeker et al., 1980;

Boyett et al., 2000). Therefore, in addition to considering networks with fixed gap junction coupling strength, we also consider networks in which g_{gap} varies depending on cell-type and location. We consider 2 types of networks: i) a linear gradient where peripheral cells have g_{gap} 15×'s stronger than center cells (termed **Strong Peripheral Gap Junction**, see Oren and Clancy (2010) who also considered this), ii) a linear gradient where center cells have g_{gap} 15×'s stronger than peripheral cells (termed **Strong Central Gap Junction**). In total, we have three different types of coupling schemes (constant g_{gap} and two types of linear gradient g_{gap}) that are not directly comparable to each other. We chose these networks to assess the robustness of our observations, and importantly to test the robustness of the subsequent reduced phase model theory in the next section.

Although there are significant differences in the three types of coupling network schemes (constant g_{gap} , Strong Peripheral Gap Junction, Strong Central Gap Junction), the following trends hold:

- The only steady-state traveling wave solution in homogeneous networks (center or peripheral) is complete synchrony.
- The only observed steady-state traveling wave in the heterogeneous network are ones that originate in the periphery and end in the center. In a given network, the frequency of this traveling wave increases with gap junction strength.
- For the same initial condition (Fig. 2C right), we observed that: the center-to-peripheral traveling wave transient persists longest in the homogeneous peripheral cell network, with the heterogeneous network generally having the shortest transient times – there are some exceptions where the homogeneous center cell network has shorter transient times than the heterogeneous network (especially with larger g_{gap} values), but the transient times are very similar in those cases.

These results will be substantiated with plots of the large-scale simulations and characterized with the reduced phase model in the next section. Specific voltage traces of the large-scale model for various network types, coupling schemes g_{gap} values, etc., are shown in Figs. 7–9 and Figs. S3–S5 (S1Text.pdf).

3.2. Reduced Phase Model Analysis of Traveling Waves

To more clearly understand the observations in the large-scale simulations, we use a reduced phase model framework. This will not only make mathematical analysis of the network dynamics feasible, but will also provide a framework for future investigations of large-scale network models of SAN tissue. The subsequent analysis relies on computing various functions from the individual Severi cell models, but did not rely on the computationally expensive step of simulating the large-scale network model.

We use the phase reduced models (see **Methods**) to approximate the behavior of the large-scale SAN network, where each cell type has an equation of the form:

$$\frac{d\theta_j}{dt} = \omega_j + \sum_k H_{j,k}(\theta_k - \theta_j) \quad (12)$$

The frequencies ω_j are all scaled by the slowest intrinsic frequency (often the center cell with $T = 0.353$ s), such that in the heterogeneous network, the center cells have $\omega = 1$ and peripheral

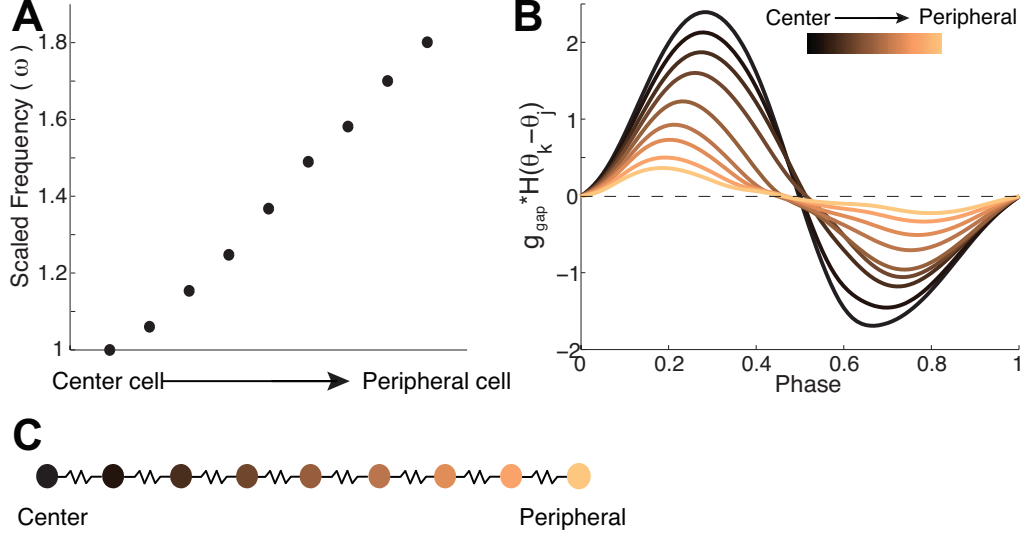


Figure 3: The phase oscillator model approximation to the large-scale Severi pacemaker model. **A)** The intrinsic frequencies were obtained from the full model and scaled by the largest period. **B)** The interaction functions $H_{j,k}$ are approximated with H_j for $k = j - 1$ and $k = j + 1$; see Eq (7). We set $g_{\text{gap}} = 1$ nS for illustration purposes. **C)** The 1D chain approximation to the full 2D model.

cells $\omega \approx 1.8$ (see Fig. 3A for the full range of possible ω values and Fig. 3B for unscaled versions of $H_{j,k}$). Note that the intrinsic period of the peripheral cell is $T = 0.196$ s.

The reduced phase model consists of a 1D chain of 9 phase oscillators with nearest neighbor coupling: $H_{j,k} \equiv 0$ unless $k = j - 1$ or $k = j + 1$ (see Fig. 3C), such that Eq. (12) for this 1D chain is re-written as:

$$\begin{aligned}
 \frac{d\theta_1}{dt} &= \omega_1 + H_{1,2}(\theta_2 - \theta_1) \\
 \frac{d\theta_j}{dt} &= \omega_j + H_{j,j-1}(\theta_{j-1} - \theta_j) + H_{j,j+1}(\theta_{j+1} - \theta_j), \text{ for } j = 2, \dots, 8 \\
 \frac{d\theta_9}{dt} &= \omega_9 + H_{9,8}(\theta_8 - \theta_9)
 \end{aligned} \tag{13}$$

This model is amenable to analysis of traveling wave dynamics (Kopell and Ermentrout, 1986; Ermentrout and Terman, 2010; Keener and Sneyd, 1998). Traveling wave solutions to this system are of the form

$$\theta_j(t) = \Omega t + \xi_j \tag{14}$$

where Ω is the ensemble (scaled) frequency of the coupled network and ξ_j represents the phase lags of each cell type (i.e., $\xi_j = 0 \forall j$ is complete synchrony). Substituting Eq. (14) into Eq. (13) gives:

$$\Omega = \omega_j + \sum_k H_{j,k}(\xi_k - \xi_j), \text{ for } j = 1, \dots, 9. \tag{15}$$

The system of 9 nonlinear equations and 10 unknowns (Ω, ξ_j) can be reduced to 9 unknowns by exploiting the periodicity of $\xi_j \in [0, 1)$, and setting $\xi_1 = 0$. Thus, if $\xi_j - \xi_{j+1} > 0$ for $j = 2, \dots, 8$

the traveling wave originates at the center ($j = 1$), and if $\xi_{j+1} - \xi_j > 0$ the traveling wave originates in the periphery (see Ermentrout and Terman (2010) for similar exposition).

Traveling wave solutions to the reduced phase model system exist (numerically) whenever the variables $(\Omega, \vec{\xi})$ satisfy the Eqs. (14)–(15). For each of the coupling schemes and all three network types (2 homogeneous, uniform heterogeneous), we found several sets of g_{gap} values where traveling wave solutions numerically existed (at least 4 for each). Solutions to Eqs. (14)–(15) were found using `fmincon` in Matlab with high precision (agreement of at least 3 decimal places in each equation).

To address the stability of traveling wave solutions when they exist, we rely on a theorem by Kopell and Ermentrout (1986); Ermentrout (1992) which provides sufficient conditions for the stability of traveling wave solutions. The theorem re-stated for these reduced phase model networks is:

Theorem 1. *The traveling wave solution $(\Omega, \vec{\xi})$ that satisfies Eq. (15) is stable if the coupled network is irreducible and $H'_{j,k}(\xi_k - \xi_j) \geq 0$.*

We prove the stability of traveling waves by applying this theorem to a range of parameter sets in the 3 network types and coupling regimes. Note that the chain of oscillators (Fig. 3C) is irreducible since every oscillator is connected, so the only condition to check is $H'_{j,k}(\xi_k - \xi_j) \geq 0$. In correspondence with the large-scale network, recall that we consider: i) constant gap junction coupling, and gradient gap junction coupling with ii) a linear gradient where peripheral cells have g_{gap} $15\times$'s stronger than center cells (termed **Strong Peripheral Gap Junction**), and iii) a linear gradient where center cells have g_{gap} $15\times$'s stronger than peripheral cells (termed **Strong Central Gap Junction**).

Synchrony is the only periodic steady state for the homogeneous networks (all center cells or all peripheral); we explain why this state is always stable. With complete synchrony, $\xi_j = 0 \forall j$ in Eq. (14), so we only have to check that $H'_{j,k}(0) \geq 0$ according to the theorem. This is easily verified in Fig. 3B, and holds for any $g_{gap} > 0$ as well as any other homogeneous network with any one of the 9 cell types. Thus, complete synchrony is always a stable state in the homogeneous networks we consider.

In the heterogeneous networks, the traveling wave solutions consist of $\xi_j > 0$, so we have to verify that $H'_{j,k}(\xi_k - \xi_j) \geq 0$ numerically to show that the solution is stable. We considered 14 total parameter sets for the heterogeneous networks where traveling wave solutions exist (5 with constant g_{gap} coupling, 4 with strong peripheral, 5 with strong central), and in all cases, the traveling wave is stable. Fig. 4 shows the smallest (left column) and largest coupling values (right column) considered, with each coupling schemes organized by row. Notice that in all instances, $H'_{j,k} > 0$, indicating that the traveling wave is stable. Stability of other heterogeneous parameter sets we consider are shown in Fig. S1 (S1Text.pdf).

The coupled reduced phase model can also qualitatively reproduce the key property of tissue frequency from the large-scale model in both uniformly coupled homogeneous (either all center or all peripheral) or heterogeneous population of SAN cells. This is demonstrated with a variety of coupling schemes and values: with constant gap junction (Fig. 5A), strong peripheral gap junction (Fig. 5B), strong central gap junction (Fig. 5C). The solid lines in Fig. 5 are the Ω from the reduced phase model, using Eq. (14) but scaled by the smallest intrinsic frequency to have units of (1/sec), while the tissue frequencies from the large-scale model (stars) are calculated by taking the average of the peak frequencies of the power spectrums of the voltage (in the last 10 s out of 20 s of biological time) for all 271 pacemaker cells.

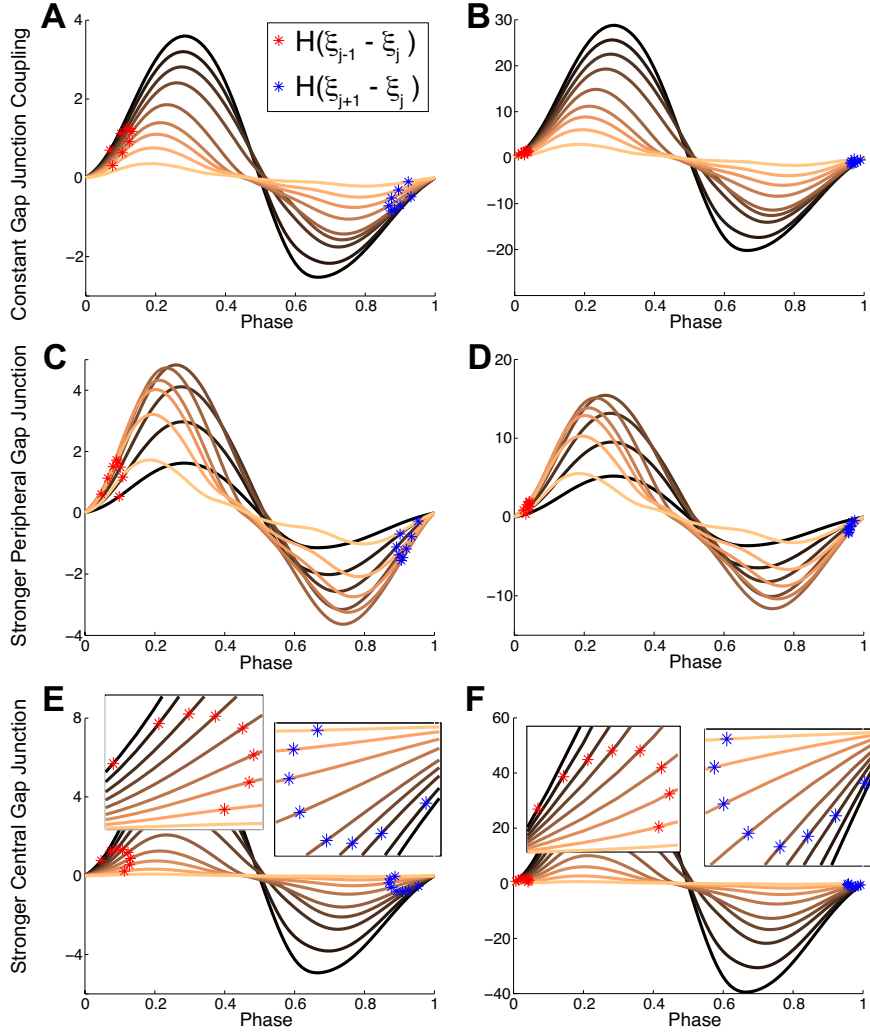


Figure 4: Existence and stability of traveling waves for heterogeneous networks. The following plots show the H -functions for a specific gap junction coupling strengths, along with calculated quantities $H_{j,k}(\xi_{j-1} - \xi_j)$ and $H_{j,k}(\xi_{j+1} - \xi_j)$. A sufficient condition for stability of the waves relies, in part, on $\frac{dH}{d\theta}(\xi_{j-1} - \xi_j) > 0$ and $\frac{dH}{d\theta}(\xi_{j+1} - \xi_j) > 0$ (see main text), which holds for all networks here. In all the regimes we explored with heterogeneous cells, traveling waves originating in peripheral cells exists and is stable. **A)** For constant gap junction coupling, with $g_{gap} = 0.25$ nS in the full large-scale network. **B)** Same as **A)** but with larger $g_{gap} = 2$ nS. **C)** Gap junction strength g_{gap} varying monotonically from center to peripheral, with largest value at the peripheral cells ($g_{gap} = 1.25/15$ nS) and smallest value at center cells ($g_{gap} = 1.25/15$ nS). **D)** Same as **C)** but with much larger coupling, $g_{gap} = 4$ nS at peripheral cells and $g_{gap} = 4/15$ nS at center cells. **E)** Gap junction strength varying monotonically, with largest at the center cells ($g_{gap} = 0.5$ nS) and smallest at peripheral cells ($g_{gap} = 0.5/15$ nS). The 2 insets are zoomed-in pictures to convincingly show that the stars are where H is increasing (i.e., $\frac{dH}{d\theta} > 0$). **F)** Same as **E)** but with much larger coupling, $g_{gap} = 4$ nS at center cells and $g_{gap} = 4/15$ nS at peripheral cells.

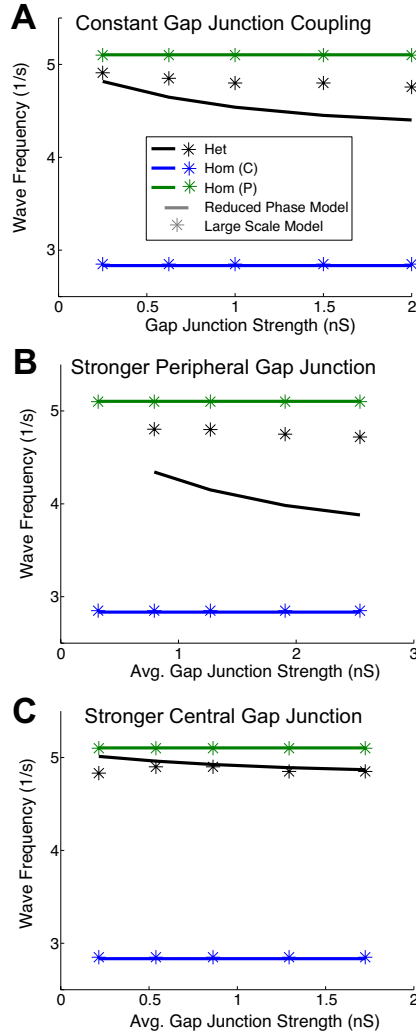


Figure 5: Reduced phase model theory captures the traveling wave frequency in the large-scale model. The ensemble traveling wave frequency in the reduced phase model (Ω in Eq. (14) scaled to 1/sec) plotted with solid lines, is compared to the traveling wave frequency of the full large-scale coupled network model (stars). We only plot network regimes where a traveling wave solution exists in the reduced phase model. In all panels, the periodic steady state for both homogeneous Center (blue) and Peripheral (green) cell networks is complete synchrony; in the heterogeneous network (black), the wave originates in the periphery and terminates somewhere near the center. **A**) For constant gap junction coupling, varying g_{gap} from 0.25 nS to 2 nS in the full large-scale network. **B**) Gap junction strength g_{gap} varying monotonically from center (weakest) to peripheral (strongest); the x-axis shows the average g_{gap} among all connected cells for a given network configuration. In the heterogeneous network, a traveling wave solution does not exist for smaller g_{gap} . **C**) Gap junction strength g_{gap} varying monotonically from center (strongest) to peripheral (weakest); x-axis has the same convention as **B**.

Although the matches between the curves (phase model) and stars (large-scale simulations) in Figure 5 are not quantitatively accurate for heterogeneous networks, the qualitative trend that

wave frequency decreases with gap junction strength is captured. The comparisons deviate most with strong peripheral (gradient coupling strength, Fig. 5B), and are most accurate with strong central (gradient coupling strength, Fig. 5C); the match with constant gap junction coupling in Figure 5A is better than B and worse than C. This is all likely due to the violation (or conformity) of the weak heterogeneity assumption in the reduced phase model. This assumption is severely violated with stronger peripheral gap junction because the larger number of peripheral cells with the hexagonal grid (Fig. 2C left) *combined* with larger g_{gap} results in a phase model with large heterogeneity from cell-type to cell-type (cell-types are grouped and averaged in the reduced phase model). Conversely, with stronger central gap junction, the larger number of peripheral cells is counter balanced by weaker g_{gap} , resulting in weaker heterogeneity from cell-type to cell-type. Note that even for relatively large coupling strengths, the deviations in wave frequency are modest, differing by less than 1 Hz.

Finally, we use the phase reduced model to characterize the transient dynamics before the coupled system settles to a stable traveling wave. A perturbation $\vec{\eta}(t)$ to a traveling wave solution $\vec{\theta}(t) = \Omega t + \vec{\xi}$ is:

$$\theta_j(t) = \Omega t + \xi_j + \eta_j(t); \quad (16)$$

the transient dynamics can be approximated by assuming perturbations are small ($\eta_j = O(\varepsilon)\forall j$); see **Methods** section for further details. This equation in matrix-vector form is (see equation (11)):

$$\frac{d\vec{\eta}}{dt} = A\vec{\eta}$$

When a traveling wave solution is stable, all but one of the eigenvalues of A have negative real part; there is a distinct zero eigenvalue $\lambda_0 = 0$ with eigenvector $\vec{1}$ that corresponds to a constant shift in the traveling wave solution – a constant shift in all variables is a perturbation that does not decay because the result is the same traveling wave solution.

Recall that the vector of perturbations can be approximated by using an eigenvector expansion (see **Methods** section). Let the eigenvectors of A be $\vec{\psi}_j$ with eigenvalues λ_j : $A\vec{\psi}_j = \lambda_j\vec{\psi}_j$. We use the initial condition from the large-scale (Fig. 2C left) mapped to the phase variable; this is well-approximated by $\vec{\eta}_0(j) = 1 - j * \frac{1}{10}$ (traveling wave starting at center) but we use the actual mapped phase value. The vector of perturbations $\vec{\eta}$ is approximated via:

$$\vec{\eta}(t) = (\vec{\psi}_1, \vec{\eta}_0) e^{\lambda_1 t} \vec{\psi}_1$$

where λ_1 is the eigenvector with large nonzero real part, and (\vec{v}, \vec{w}) is the usual inner product. In the Supplementary Material (S1Text.pdf), we show that this solution is numerically the same as the full eigenvector expansion (see Fig. S2 in S1Text.pdf). The times to the steady-state traveling wave solutions are approximated by determining when the perturbations decay to a specified tolerance: $\|\vec{\eta}(t)\| < \epsilon$. In all figures (6A, C, E, 7–9), we use $\epsilon = 1 \times 10^{-4}$.

To numerically determine the time point at which the transients have decayed in the large-scale simulations, we check that the time course of the voltage in a period T_c (inverse of frequency calculated in Fig. 5 (stars)) is within a specified tolerance of the next cycle; the transient time is over only when the voltages match for all 271 cells:

$$\arg \min_t \left\{ \frac{|v_j(t) - v_j(t + T_c)|}{M_k} < \epsilon \left| \max_t(v_j(t)) - \min_t(v_j(t)) \right|, \quad \forall j = 1, \dots, 271 \text{ cells} \right\}$$

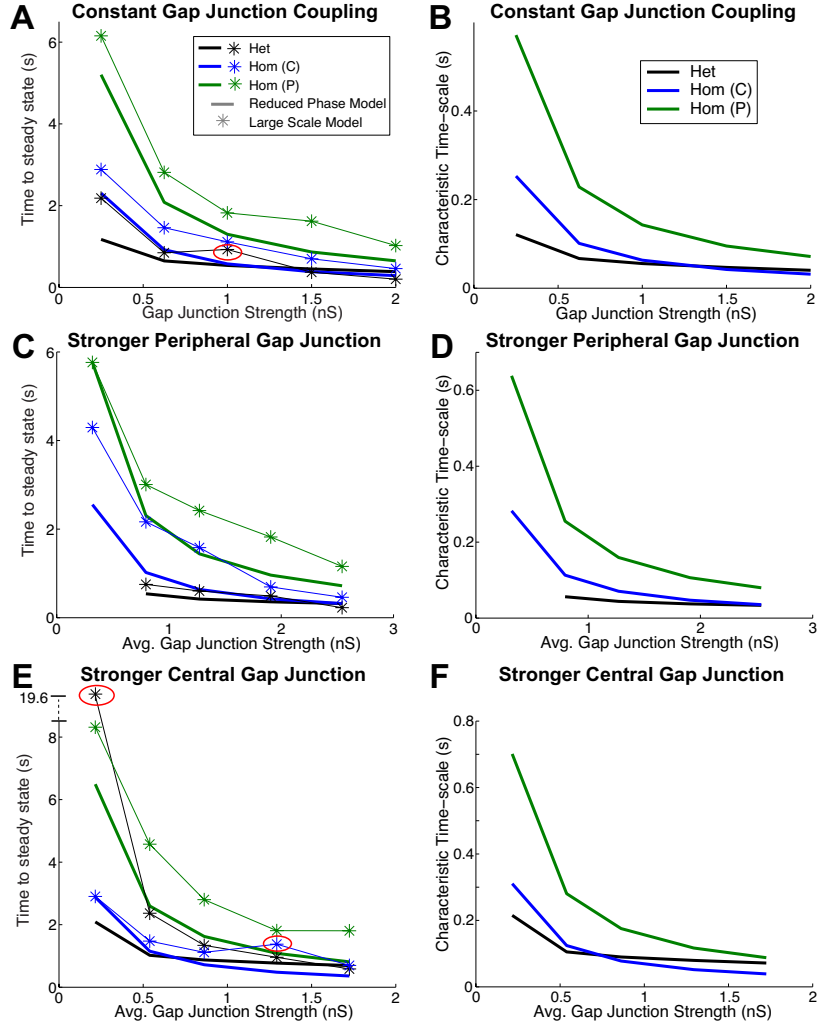


Figure 6: Reduced phase model theory captures the transient times before settling to steady-state traveling waves. Left Column: for a given network configuration with initial condition primed to center-to-peripheral traveling waves (Fig. 2C right), the transient times from largest to smallest are generally: homogeneous peripheral cell network (green), homogeneous center cell network (blue), heterogeneous network (black). As coupling strength increases, transient times decrease and the differences between blue and black are diminished. Although the match between large-scale networks (stars) and reduced phase model (solid curves) is not always precise, the qualitative trends are captured. **A, B**) For constant gap junction coupling, varying g_{gap} from 0.25 nS to 2 nS in the full large-scale network. **C, D**) Gap junction strength g_{gap} varying monotonically from center (weakest) to peripheral (strongest); the x-axis shows the average g_{gap} among all connected cells for a given network configuration. **E, F**) Gap junction strength g_{gap} varying monotonically from center (strongest) to peripheral (weakest); x-axis has the same convention as **C, D**. The 3 red ovals are when the effects from the boundaries of the hexagonal grid persist so that the 1D chain is a bad approximation – see Supplementary Material (from top to bottom: vidx_Het_g3_s3.mp4, vidx_Het_g2_s2.mp4, vidx_HomC_g33_s3.mp4 in S2.zip). The right column shows the characteristic time-scale ($(|\lambda_1|)^{-1}$, where λ_1 is the largest negative eigenvector of A ; see Eq. (10) but rescaled to seconds) as a measure transient time dynamics.

where M_k =number of time points in a period, and $\mathbf{e} = 1 \times 10^{-3}$ for the two homogeneous networks and $\mathbf{e} = 1.7 \times 10^{-3}$ for all heterogeneous networks² (black stars). See Figure 6A, C, E for comparisons of the transient times.

We remark that numerically calculating a precise time when the large-scale model reaches a steady-state traveling wave solution is tenuous, because the results are sensitive to the tolerance. Yet despite this, we find great qualitative matches between the reduced phase model and the large-scale network with relatively generic tolerances. Indeed, Figure 6A, C, E shows the match between phase model (thick lines) and large-scale networks (stars connected by lines) can be accurate. When the match is not precise, the following trends are captured: homogeneous peripheral cells (green) have longer transients, followed by homogeneous center (blue), then heterogeneous (black); transient times decrease with coupling strength; homogeneous center and heterogeneous networks have similar transient time with stronger coupling. The 3 red ovals in Fig. 6 left column are for conditions for which boundary effects influence transient times (see Supplementary Material referenced in Fig. 6 caption). Because our grid is truly 2-dimensional (as opposed to radially symmetric grids where nearest neighbor coupling spans disparate Euclidean distances), such boundary effects cannot easily be removed.

A common way to quantify the duration of transient dynamics is to consider the *characteristic time-scale*, which for a linear system is defined as the inverse of the modulus of the eigenvector with largest (negative) real part $|\lambda_1|^{-1}$ of A . This transient time measure does not depend on a particular initial condition or numerical tolerance. The characteristic time-scale from the reduced phase model is shown in the right column of Fig. 6B, D, F, and it does indeed capture all of the trends in both the reduced phase model and large-scale networks: homogeneous peripheral cell network has the longest transients, transient time decreases as coupling strength increases, heterogeneous network has the shortest transient time with weaker coupling, homogeneous central cell network has similar transient times as the heterogeneous networks with stronger coupling.

The results in Figure 6 are further detailed with plots of the voltage trajectories, along with the transient times calculated both via the reduced phase model (cyan arrows, Figs. 7–9) and large-scale simulation (blue arrows, Figs. 7–9). In Figures 7–9, it is apparent that both transient time estimations from the the reduced phase model and the large-scale simulations are relatively accurate. The only exceptions are perhaps when the large-scale simulations exhibit behavior that cannot be well-approximated by a 1D chain of oscillators (i.e., plots that correspond to the 3 red ovals in Fig. 6 left column). The constant gap junction coupling scheme is shown in Figure 7, with each row consisting of a particular cell distribution (i.e., heterogeneous or homogeneous) and each column has the same set of g_{gap} values. We again see that for a given coupling scheme (i.e., column) the homogeneous peripheral cell network has the longest transient times, generally followed by the homogeneous center cell network, and then the heterogeneous network. Figure 8 shows the gradient g_{gap} with stronger peripheral coupling, and Figure 9 is with stronger central coupling. See Figures S3–S5 (S1Text.pdf) for other parameter values not shown in Figures 7–9.

In all of the large-scale networks considered so far, the corresponding phase model showed that traveling wave solutions exist. However, there are network regimes where traveling wave solutions cannot be found with sophisticated optimization routines, and thus traveling wave solutions likely do not exist. An example of this is the heterogeneous network with stronger peripheral gap junction coupling where $g_{gap} \in \left[\frac{0.5}{15}, 0.5 \right]$ nS (see Fig. 10). In this network, we find

²This tolerance was the minimum that gave reasonable results when incrementing by 1×10^{-4} from $\mathbf{e} = 1 \times 10^{-3}$. One data point corresponding to strong central coupling in the heterogeneous network and small $g_{gap} \in \left[\frac{0.5}{15}, 0.5 \right]$ nS (Fig. 6C black star) did not yield reasonable transient times for similar valued tolerances; see vidx_Het.g2.s2.mp4 in S2.zip.

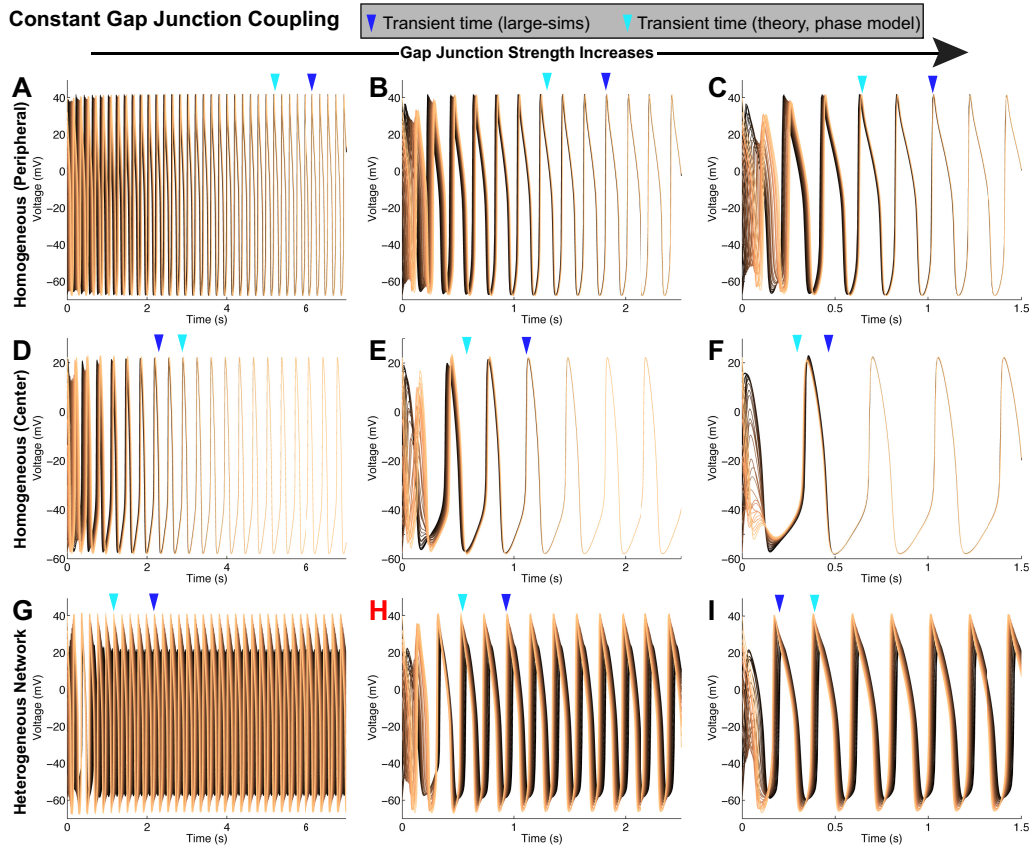


Figure 7: Voltage trajectories in large-scale model plotted with the theoretical transient time (reduced phase model) and large-scale transient time: with constant gap junction coupling. By inspection, the transient times from the reduced phase model (cyan arrow) and large-scale model (blue arrow) appears qualitatively accurate. Each column has different coupling strengths, each row is a particular type of network. Left column (**A**, **D**, **G**) is with $g_{gap} = 0.25$ nS. Middle column (**B**, **E**, **H**) is with $g_{gap} = 1$ nS. Right column (**C**, **F**, **I**) is with $g_{gap} = 2$ nS. **A**–**C**) The homogeneous network of peripheral cells. **D**–**F**) The homogeneous network of center cells. **G**–**I**) The heterogeneous network consisting of 9 different cell types. In each column, the transient generally last longest for homogeneous peripheral cell networks (top row), following by homogeneous center cells, with the heterogeneous network having the shortest transient. The label **H** is red to correspond with the red oval in Figure 6A.

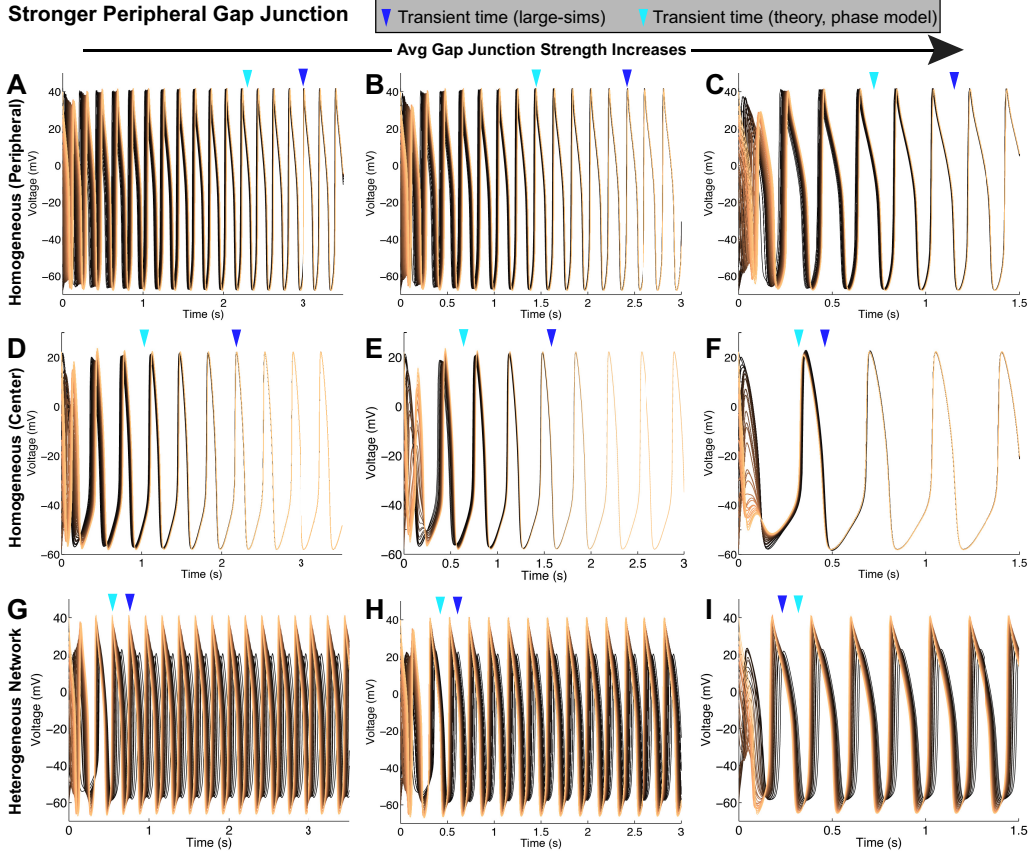


Figure 8: Voltage trajectories in large-scale model plotted with the theoretical transient time (reduced phase model) and large-scale transient time: with strong peripheral coupling. Again by inspection, the transient times from the reduced phase model (cyan arrow) and large-scale model (blue arrow) appears qualitatively accurate. Each column has different coupling strengths, each row is a particular type of network (same format as Fig. 7). Left column (A, D, G) is with $g_{gap} \in (0.625, 0.625)$ nS. Middle column (B, E, H) is with $g_{gap} \in (\frac{2}{15}, 2)$ nS. Right column (C, F, I) is with $g_{gap} \in (\frac{4}{15}, 4)$ nS. In each column, the transient generally last longest for homogeneous peripheral cell networks (top row), following by homogeneous center cells, with the heterogeneous network having the shortest transient.

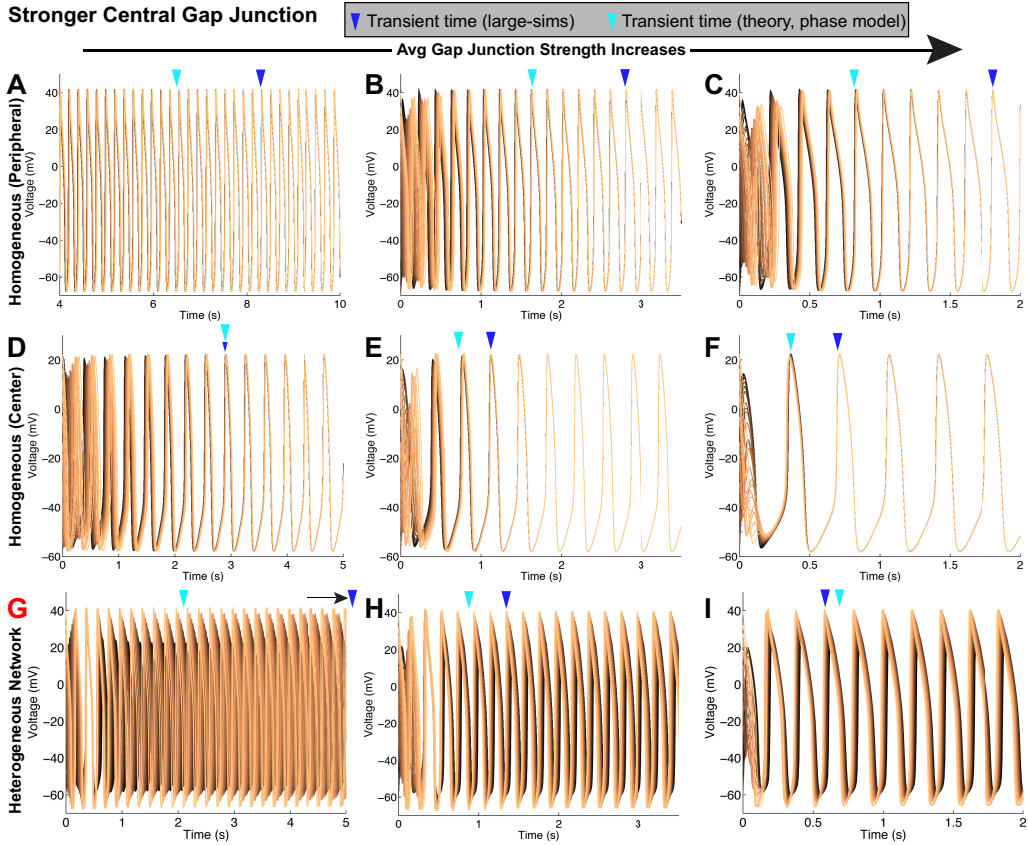


Figure 9: Voltage trajectories in large-scale model plotted with the theoretical transient time (reduced phase model) and large-scale transient time: with strong central coupling. Again by inspection, the transient times from the reduced phase model (cyan arrow) and large-scale model (blue arrow) appears qualitatively accurate. Each column has different coupling strengths, each row is a particular type of network (same format as Fig. 7). Left column (A, D, G) is with $g_{gap} \in \left(\frac{0.625}{15}, 0.625\right)$ nS. Middle column (B, E, H) is with $g_{gap} \in \left(\frac{2}{15}, 2\right)$ nS. Right column (C, F, I) is with $g_{gap} \in \left(\frac{4}{15}, 4\right)$ nS. In each column, the transient generally last longest for homogeneous peripheral cell networks (top row), following by homogeneous center cells, with the heterogeneous network having the shortest transient. The label G is red to correspond with the top red oval in Figure 6E.

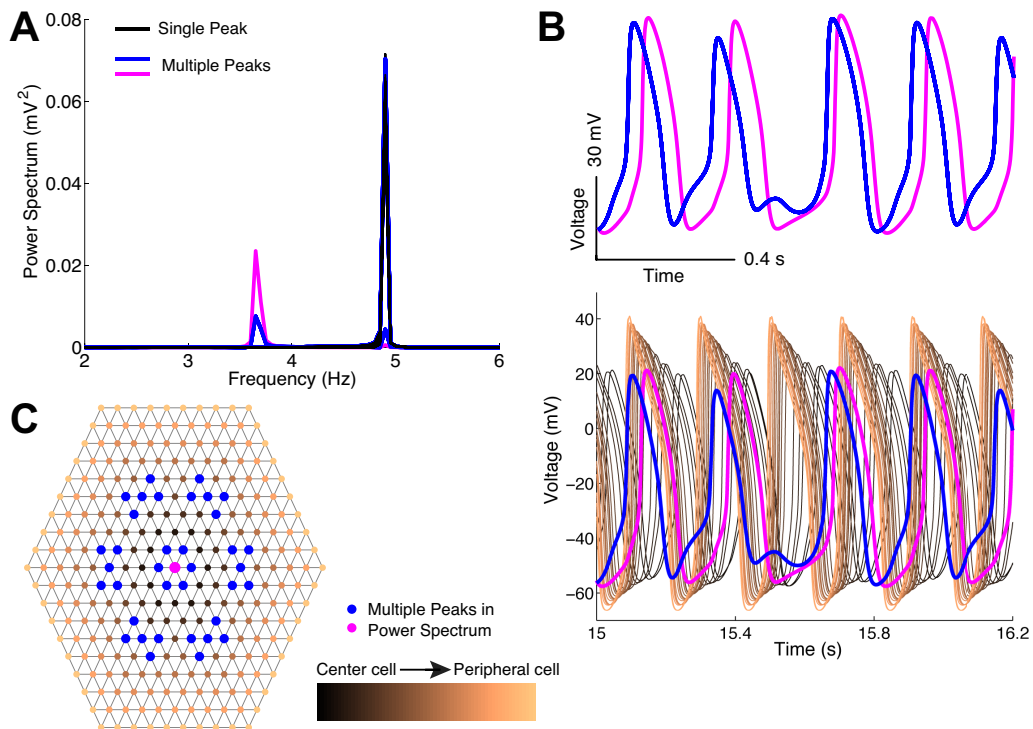


Figure 10: A network where a traveling wave solution does not exist. The heterogeneous network has stronger peripheral gap junction coupling, with $g_{gap} \in \left[\frac{0.5}{15}, 0.5\right]$ nS. **A)** Power spectrums of all 271 voltage traces (after transients have decayed, from 10 s–20 s). There are cells (37 total in blue and magenta) with multiple peaks in the power spectrum, a signature of multiple time-scales; in contrast to all of the other prior networks we considered. **B)** Two types of voltage traces that have irregular dynamics (different spike widths, heights, etc. from cycle to cycle); all but the center most cell (magenta) have the blue voltage traces. **C)** The spatial location of the cells with multiple time-scales in voltage. See Supplementary Material (vidx_Het_g2_s1.mp4 in S2.zip).

that the power spectrum of all 271 voltage traces (after transients have decayed) have a subset of 37 cells with multiple peaks (Fig. 10A). This suggests that the voltage time course for some cells have multiple time-scales, in contrast to previously described networks thus far, for which the voltage trace power spectrum is unimodal for all cells. Inspection of the voltage traces indeed shows irregularities from cycle to cycle (Fig. 10B), with different spike widths, heights, etc. for the subset of cells with multi-modal power spectrums. The voltage trajectories of these ‘irregular’ cells are all synchronized except for the center most cell (see Fig. 10C for the spatial location). Importantly, the failure to find a traveling wave solution in the reduced model is consistent with the large-scale simulations, where the persistent solution is indeed not a traveling wave solution, which demonstrates that the reduced model formulation can provide an approach to identify regimes of irregular voltage dynamics.

4. Discussion

In this study, we demonstrate the utility of the mathematical framework of coupled phase oscillators to mechanistically characterize the spatio-temporal dynamics of a large locally coupled network of heterogeneous sinoatrial node (SAN) cells, for which the individual cell models themselves are complex with many state variables and compartments. Summarizing our approach and main findings, we implemented a recently developed model of the central pacemaker cells in the SAN (Severi et al., 2012) and modified model parameters to capture a heterogeneous population of pacemaker cells to yield a large-scale SAN network tissue model. In electrically (gap junction) coupled tissue consisting of hundreds of pacemaker cells, we observed vastly different ‘steady-state’ or persistent behavior for tissue comprised of different intrinsic cell types. We found that the persistent behavior (synchrony for homogeneous cell network or peripheral-to-center waves for heterogeneous networks) was highly robust, even as both coupling schemes and gap junction strengths varied.

To explain observations in the large-scale models, we applied a reduced model framework consisting of a 1D chain of phase oscillators that accounted for different cell types and coupling strengths from the full 2D network. Importantly, the reduced phase model relied on quantities (i.e., intrinsic frequencies, cell-to-cell interactions) from the individual pacemaker cell model but did not rely on computationally expensive simulations of the large-scale model. This framework successfully captured when traveling waves exist, uncovered the stability of these persistent states, and was used to calculate the transient times – all in a variety of network types, and coupling schemes and strengths. In addition to requiring less computational resources to capture the large-scale phenomena, the phase models enabled our detailed mathematical analysis.

While this general analysis has been applied to minimal cardiac cell models, to our knowledge, our analysis of a complex and highly detailed biophysical representation of pacemaker cells is unique and novel. For example, see section 14.2 in Keener and Sneyd (1998), who described the basis of a phase model approach for a minimal cardiac pacemaker network with only 2 state variables per cell. In particular, our application is valuable, as it establishes a framework for future mechanistic investigations of irregular SAN electrical function, driven by defective ion channel gating or expression. Ion channel dysfunction (e.g., reduced funny current associated with sick sinus syndrome (Schweizer et al., 2014)) can be incorporated into the underlying pacemaker cell models and subsequent reduced phase model stability can be predicted. Moreover, the application of reduced phase models to heterogeneous networks has been scarce; see (Ly, 2014; Zhou et al., 2013; Ashwin et al., 2016) for a few exceptions we are aware of. Strogatz

and others (Mirolo and Strogatz, 1990; Acebrón et al., 2005) considered heterogeneous intrinsic frequencies but not heterogeneous coupling functions in coupled phase models.

Our work could potentially elucidate large simulation studies in which center-to-peripheral traveling waves are observed. We do observe central-to-peripheral traveling waves, but only transiently, and the transient times strongly depend on cell types in the network. Specifically, the transient times were generally longer for homogeneous networks than heterogeneous. In principle, this framework could be applied to other models (Zhang et al., 2000; Oren and Clancy, 2010) to mathematically characterize the steady-states and transient times. We note that Oren and Clancy (2010) argued that more realistic center-to-peripheral traveling waves only occurred in homogeneous networks, and not in heterogeneous networks.

We only applied the reduced phase model theory to conditions for which steady-state traveling wave solutions exist and are stable. However, we have seen that there are regimes for which traveling wave solutions do not exist in the phase model (nor in the large-scale model) and the cell behavior is irregular from cycle to cycle (Fig. 10). Extending the phase oscillator framework to these complex dynamics and beyond is a promising area of future research, especially given the implications for these dynamics on cardiac arrhythmias and other disease. We are also interested in developing reduced phase model methods to analyze cardiac SAN tissue models that incorporate further SAN cell population heterogeneity, including fibroblast cells and the transition between the pacemaker region to the atrium, which may yield stable center-to-peripheral traveling waves.

As experimental techniques advance and single cell models naturally increase in complexity with more variables and parameters, the necessity of tractable and insightful models will be dire. We have demonstrated that these reduced phase models and corresponding mathematical analysis are valuable for studying large realistic coupled cardiac networks. For example, as more accurate data become available about the distribution of pacemaker cells' intrinsic frequency and cell coupling, this framework can be used to probe the spatio-temporal dynamics efficiently rather than performing computationally intensive simulations for a wide range of parameters. Indeed, the only limitations of this analysis is that the cells intrinsically oscillate, the heterogeneity among neighboring cells is relatively weak, and the coupling weak, criteria generally satisfied with electrically coupled pacemaker cells in SAN tissue.

Appendix A. Detailed equations for the large-scale model

Here we provide more details for the full pacemaker cell models (Eq. (1)). For the complete details, we provide the Matlab code for the models, freely available at [GitHub](#). There are 31 total dynamic variables with their own differential equation for *each* cell, and many auxiliary functions.

The voltages are in units of milli-Volts (mV). The sodium current is:

$$I_{Na}(v) = g_{Na}m^3h(v - E_{Na}) \quad (\text{A.1})$$

$$E_{Na} = \frac{RT}{F} \ln(Na_o/Na_i) \quad (\text{A.2})$$

$$\frac{dx}{dt} = \alpha_x(v)(1 - x) - \beta_x(v)x, \text{ where } x \in \{m, h\} \quad (\text{A.3})$$

where g_{Na} is the conductance (varies, see Table 2), m and h are the sodium activation and inactivation variables, R is the universal gas constant, F is Faraday's constant, T is temperature in

Kelvin (310, or 36.85° C), $Na_o = 140$ mM is the extracellular sodium concentration; Na_i is the dynamic intracellular concentration with its own differential equation; $\alpha_m(v)$, $\alpha_h(v)$, $\beta_m(v)$, $\beta_h(v)$ are standard gating variables.

The funny current is:

$$I_f(v) = g_{f,Na} y_f^2 K_o / (K_o + 45) (v - E_{Na}) + g_{f,K} y_f^2 K_o / (K_o + 45) (v - E_K) \quad (A.4)$$

$$E_K = \frac{RT}{F} \ln(K_o / K_i) \approx -86.96 \text{ mV} \quad (A.5)$$

$$\frac{d(y_f)}{dt} = (y_{f,\infty}(v) - y_f) / \tau_{yf}(v) \quad (A.6)$$

where $g_{f,Na}$, $g_{f,K}$ are the conductances (varies, see Table 2); $K_o = 5.4$ mM is the extracellular potassium concentration, $K_i = 140$ mM is the intracellular potassium concentration.

The transient outward potassium current is:

$$I_{to}(v) = g_{to} q * r * (v - E_K) \quad (A.7)$$

$$\frac{dx}{dt} = (x_{\infty}(v) - x) / \tau_x(v), \text{ where } x \in \{q, r\} \quad (A.8)$$

with $g_{to} = 0.002 \mu\text{S}$; for this and other currents, the steady state functions $x_{\infty}(v)$ and time constant $\tau_x(v)$ are what were used in Severi et al. (2012).

The L-type calcium current is:

$$I_{Ca,L} = I_{si,Ca} + I_{si,K} + I_{si,Na} \quad (A.9)$$

$$I_{si,Ca} = \frac{2P_{CaL} * v}{\frac{RT}{F} (1 - \exp(-2v \frac{F}{RT}))} (Ca_{sub} - Ca_o \exp(-2v \frac{F}{RT})) * d_L * f_L * f_{Ca} \quad (A.10)$$

$$I_{si,K} = \frac{3.65 \times 10^{-4} P_{CaL} * v}{\frac{RT}{F} (1 - \exp(-v \frac{F}{RT}))} (K_i - K_o \exp(-v \frac{F}{RT})) * d_L * f_L * f_{Ca} \quad (A.11)$$

$$I_{si,Na} = \frac{1.85 \times 10^{-5} P_{CaL} * v}{\frac{RT}{F} (1 - \exp(-v \frac{F}{RT}))} (Na_i - Na_o \exp(-v \frac{F}{RT})) * d_L * f_L * f_{Ca} \quad (A.12)$$

$$\frac{dx}{dt} = (x_{\infty}(v) - x) / \tau_x(v), \text{ where } x \in \{d_L, f_L\} \quad (A.13)$$

$$\frac{d(f_{Ca})}{dt} = (f_{Ca,\infty}(Ca_{sub}) - f_{Ca}) / \tau_{fCa}(Ca_{sub}) \quad (A.14)$$

where P_{CaL} is the conductance (varies, see Table 2), $Ca_o = 1.8$ mM is the extracellular calcium concentration, Ca_{sub} is the dynamic subspace calcium concentration with its own differential equation.

The T-type calcium current is:

$$I_{Ca,T} = \frac{2P_{CaT} * v}{\frac{RT}{F} (1 - \exp(-2v \frac{F}{RT}))} (Ca_{sub} - Ca_o \exp(-2v \frac{F}{RT})) * d_T * f_T \quad (A.15)$$

$$\frac{dx}{dt} = (x_{\infty}(v) - x) / \tau_x(v), \text{ where } x \in \{d_T, f_T\} \quad (A.16)$$

where P_{CaT} is the conductance (varies, see Table 2).

The rapid delayed rectifier K^+ and slow delayed rectifier K^+ currents are:

$$I_{Kr} = g_{Kr} * (0.9 * p_{aF} + 0.1 * p_{aS}) * p_i * (v - E_K) \quad (\text{A.17})$$

$$I_{Ks} = g_{Ks} * n^2 * (v - E_K) \quad (\text{A.18})$$

$$\frac{dx}{dt} = (x_\infty(v) - x) / \tau_x(v), \text{ where } x \in \{p_{aF}, p_{aS}, p_i, n\} \quad (\text{A.19})$$

where both g_{Kr} and g_{Ks} conductances vary by cell type (see Table 2).

The sodium-potassium pump current $I_{Na,K}$ and sodium-calcium exchanger current $I_{Na,Ca}$ are:

$$I_{Na,K} = \frac{g_{NaK}}{(1 + 1.4/K_o)^{1.2} (1 + 14/Na_i)^{1.3} (1 + \exp(-(v - E_{Na} + 110)/20))} \quad (\text{A.20})$$

$$I_{Na,Ca} = g_{NaCa} \frac{x_2 k_{21} - x_1 k_{12}}{x_1 + x_2 + x_3 + x_4} \quad (\text{A.21})$$

The components x_1, \dots, x_4 and k_{21}, k_{12} represent the detailed calcium dynamics in the sarcoplasmic reticulum (SR), myoplasm, junctional SR, subspace SR, as well as outside of the cell. We omit the rest of the equations and functions due to their complexity and point the interested reader to our freely available computer code. We alter cell length and cell radius for different cell types, that in turns effects the cell volume, submembrane space volume, myoplasmic volume, junctional SR volume, network SR volume, which all effect the calcium dynamics.

The values for g_{NaK} and g_{NaCa} for the 9 different cells were manually altered to insure ion homeostasis and a stable limit cycle in the uncoupled cells, the values are listed in Table 3.

Funding

CL is supported by a grant from the Simons Foundation (# 355173).

Acknowledgements

The authors acknowledge and thank the Virginia Commonwealth University Center for High Performance Computing (CHiPC) for use of the Teal cluster to perform numerical simulations.

Supplementary Material

S1Text.pdf – Supplementary Figures

A PDF files that contains 5 extra figures that expound on Figures 4, **6B,D,F**, and 7–9.

S2.zip – Movies

A zip file containing several movie files (.mp4) showing the voltage evolution on the 2D hexagonal grid. Naming convention:

vidx_[Het/HomC/HomP]_io_g[2/22/3/33/4]_s[1/2/3].mp4

Het is with all cell types (heterogeneous), HomC is a homogeneous network with all center cells, HomP is a homogeneous network with all peripheral cells.

s1: gradient gap strength with peripheral having 15X larger strength than center.

s2: gradient gap strength with center having 15X larger strength than peripheral.

s3: constant gap strength throughout.

$g_2=0.25$ nS ([0.5/15,0.5] nS range of g_{gap} when gradient gap strength s_1 & s_2)
 $g_2=0.625$ nS ([1.25/15,1.25] nS range with gradient gap schemes)
 $g_3=1$ nS ([2/15,2] nS range with gradient gap schemes)
 $g_3=1.5$ nS ([3/15,3] nS range with gradient gap schemes)
 $g_4=2$ nS ([4/15,4] nS range with gradient gap schemes)

References

References

- Acebrón, J. A., Bonilla, L. L., Vicente, C. J. P., Ritort, F., Spigler, R., 2005. The kuramoto model: A simple paradigm for synchronization phenomena. *Reviews of modern physics* 77 (1), 137.
- Arevalo, H. J., Boyle, P. M., Trayanova, N. A., 2016. Computational rabbit models to investigate the initiation, perpetuation, and termination of ventricular arrhythmia. *Progress in biophysics and molecular biology* 121 (2), 185–194.
- Ashwin, P., Coombes, S., Nicks, R., 2016. Mathematical frameworks for oscillatory network dynamics in neuroscience. *The Journal of Mathematical Neuroscience* 6 (1), 2.
- Bleeker, W. K., Mackaay, A. J., Masson-Pévet, M., Bouman, L. N., Becker, A. E., 1980. Functional and morphological organization of the rabbit sinus node. *Circulation research* 46 (1), 11–22.
- Bouman, L., Jongsma, H., 1986. Structure and function of the sino-atrial node: a review. *European heart journal* 7 (2), 94–104.
- Boyett, M. R., Honjo, H., Kodama, I., 2000. The sinoatrial node, a heterogeneous pacemaker structure. *Cardiovascular research* 47 (4), 658–687.
- Csepe, T. A., Zhao, J., Hansen, B. J., Li, N., Sul, L. V., Lim, P., Wang, Y., Simonetti, O. P., Kilic, A., Mohler, P. J., et al., 2016. Human sinoatrial node structure: 3d microanatomy of sinoatrial conduction pathways. *Progress in biophysics and molecular biology* 120 (1), 164–178.
- Efimov, I. R., Fedorov, V. V., Joung, B., Lin, S.-F., 2010. Mapping cardiac pacemaker circuits. *Circulation research* 106 (2), 255–271.
- Ermentrout, B., 2002. *Simulating, analyzing, and animating dynamical systems: a guide to XPPAUT for researchers and students*. SIAM.
- Ermentrout, G. B., 1992. Stable periodic solutions to discrete and continuum arrays of weakly coupled nonlinear oscillators. *SIAM Journal on Applied Mathematics* 52 (6), 1665–1687.
- Ermentrout, G. B., Terman, D. H., 2010. *Mathematical foundations of neuroscience*. Vol. 35. Springer Science & Business Media.
- Fedorov, V. V., Chang, R., Glukhov, A. V., Kosteki, G., Janks, D., Schuessler, R. B., Efimov, I. R., 2010. Complex interactions between the sinoatrial node and atrium during reentrant arrhythmias in the canine heart. *Circulation* 122 (8), 782–789.
- Fedorov, V. V., Glukhov, A. V., Chang, R., 2012. Conduction barriers and pathways of the sinoatrial pacemaker complex: their role in normal rhythm and atrial arrhythmias. *American Journal of Physiology-Heart and Circulatory Physiology* 302 (9), H1773–H1783.
- Fedorov, V. V., Schuessler, R. B., Hemphill, M., Ambrosi, C. M., Chang, R., Voloshina, A. S., Brown, K., Hucker, W. J., Efimov, I. R., 2009. Structural and functional evidence for discrete exit pathways that connect the canine sinoatrial node and atria. *Circulation research* 104 (7), 915–923.
- Glukhov, A. V., Hage, L. T., Hansen, B. J., Pedraza-Toscano, A., Vargas-Pinto, P., Hamlin, R. L., Weiss, R., Carnes, C. A., Billman, G. E., Fedorov, V. V., 2013. Sinoatrial node reentry in a canine chronic left ventricular infarct model: The role of intranodal fibrosis and heterogeneity of refractoriness. *Circulation: Arrhythmia and Electrophysiology*, CIRCEP-113.
- Greer-Short, A., George, S. A., Poelzing, S., Weinberg, S. H., 2017. Revealing the concealed nature of long-qt type 3 syndrome. *Circulation: Arrhythmia and Electrophysiology* 10 (2), e004400.
- Honjo, H., Boyett, M., Kodama, I., Toyama, J., 1996. Correlation between electrical activity and the size of rabbit sino-atrial node cells. *The Journal of Physiology* 496 (3), 795–808.
- Keener, J., Sneyd, J., 1998. *Mathematical physiology*. Interdisciplinary applied mathematics, vol. 8. Springer-Verlag, New York.
- Kodama, I., Nikmaram, M., Boyett, M., Suzuki, R., Honjo, H., Owen, J., 1997. Regional differences in the role of the Ca^{2+} and Na^{+} currents in pacemaker activity in the sinoatrial node. *American Journal of Physiology-Heart and Circulatory Physiology* 272 (6), H2793–H2806.
- Kopell, N., Ermentrout, G., 1986. Symmetry and phaselocking in chains of weakly coupled oscillators. *Communications on Pure and Applied Mathematics* 39 (5), 623–660.

- Kuramoto, Y., 2012. Chemical oscillations, waves, and turbulence. Vol. 19. Springer Science & Business Media.
- Kurata, Y., Hisatome, I., Imanishi, S., Shibamoto, T., 2002. Dynamical description of sinoatrial node pacemaking: improved mathematical model for primary pacemaker cell. *American Journal of Physiology-Heart and Circulatory Physiology* 283 (5), H2074–H2101.
- Li, N., Csepe, T. A., Hansen, B. J., Dobrzynski, H., Higgins, R. S., Kilic, A., Mohler, P. J., Janssen, P. M., Rosen, M. R., Biesiadecki, B. J., et al., 2015. Molecular mapping of sinoatrial node hcn channel expression in the human heart. *Circulation: Arrhythmia and Electrophysiology, CIRCEP*–115.
- Li, N., Hansen, B. J., Csepe, T. A., Zhao, J., Ignozzi, A. J., Sul, L. V., Zakharkin, S. O., Kalyanasundaram, A., Davis, J. P., Biesiadecki, B. J., et al., 2017. Redundant and diverse intranodal pacemakers and conduction pathways protect the human sinoatrial node from failure. *Science translational medicine* 9 (400), eaam5607.
- Ly, C., 2014. Dynamics of coupled noisy neural oscillators with heterogeneous phase resetting curves. *SIAM Journal on Applied Dynamical Systems* 13, 1733–1755.
- Ly, C., Ermentrout, G. B., 2010. Analysis of recurrent networks of pulse-coupled noisy neural oscillators. *SIAM Journal on Applied Dynamical Systems* 9, 113–137.
- Masson-Pévet, M., Bleeker, W. K., Gros, D., 1979. The plasma membrane of leading pacemaker cells in the rabbit sinus node: a qualitative and quantitative ultrastructural analysis. *Circulation Research* 45 (5), 621–629.
- Michaels, D. C., Matyas, E. P., Jalife, J., 1987. Mechanisms of sinoatrial pacemaker synchronization: a new hypothesis. *Circulation Research* 61 (5), 704–714.
- Mirollo, R. E., Strogatz, S. H., 1990. Synchronization of pulse-coupled biological oscillators. *SIAM Journal on Applied Mathematics* 50 (6), 1645–1662.
- Oren, R. V., Clancy, C. E., 2010. Determinants of heterogeneity, excitation and conduction in the sinoatrial node: a model study. *PLoS computational biology* 6 (12), e1001041.
- Phadumdeo, V. M., Weinberg, S. H., 2018. Heart rate variability alters cardiac repolarization and electromechanical dynamics. *Journal of theoretical biology*.
- Schultheiss, N. W., Prinz, A. A., Butera, R. J., 2011. Phase response curves in neuroscience: theory, experiment, and analysis. Springer Science & Business Media.
- Schweizer, P. A., Schröter, J., Greiner, S., Haas, J., Yampolsky, P., Mereles, D., Buss, S. J., Seyler, C., Bruehl, C., Draguhn, A., et al., 2014. The symptom complex of familial sinus node dysfunction and myocardial noncompaction is associated with mutations in the hcn4 channel. *Journal of the American College of Cardiology* 64 (8), 757–767.
- Severi, S., Fantini, M., Charawi, L. A., DiFrancesco, D., 2012. An updated computational model of rabbit sinoatrial action potential to investigate the mechanisms of heart rate modulation. *The Journal of physiology* 590 (18), 4483–4499.
- Verheijck, E. E., Wessels, A., van Ginneken, A. C., Bourier, J., Markman, M. W., Vermeulen, J. L., de Bakker, J. M., Lamers, W. H., Opthof, T., Bouman, L. N., 1998. Distribution of atrial and nodal cells within the rabbit sinoatrial node: models of sinoatrial transition. *Circulation* 97 (16), 1623–1631.
- Wilders, R., 2007. Computer modelling of the sinoatrial node. *Medical & biological engineering & computing* 45 (2), 189–207.
- Winfree, A. T., 1967. Biological rhythms and the behavior of populations of coupled oscillators. *Journal of theoretical biology* 16 (1), 15–42.
- Winfree, A. T., 1970. Integrated view of resetting a circadian clock. *Journal of Theoretical Biology* 28 (3), 327–374.
- Zeitzer, J. M., Dijk, D.-J., Kronauer, R. E., Brown, E. N., Czeisler, C. A., 2000. Sensitivity of the human circadian pacemaker to nocturnal light: melatonin phase resetting and suppression. *The Journal of physiology* 526 (3), 695–702.
- Zhang, H., Holden, A., Kodama, I., Honjo, H., Lei, M., Varghese, T., Boyett, M., 2000. Mathematical models of action potentials in the periphery and center of the rabbit sinoatrial node. *American Journal of Physiology-Heart and Circulatory Physiology* 279 (1), H397–H421.
- Zhou, P., Burton, S., Urban, N., Ermentrout, G. B., 2013. Impact of neuronal heterogeneity on correlated colored noise-induced synchronization. *Frontiers in computational neuroscience* 7, 113.

Table 2: Parameter values for the pacemaker cell model. All parameters changes proportionally ($\min * (1 - s) + \max * s$, $s = 0$ for Center and $s = 1$ for Peripheral) except the NaK pump and NaCa exchanger conductances, which were manually altered to insure a stable limit cycle (see Table 3 for these and s values)). See equations in Appendix A for further details.

Parameter	Range (Center→Peripheral)	Unit	Factor: Peripheral/Center
Capacitance, C	[32,65]	pico-Farads (pF)	2.03
Cell Length	[70,86]	micrometer (μm)	1.23
Cell Radius	[4,6]	micrometer (μm)	1.5
Na^+ (funny current) Conductance, $g_{f,Na}$	[0.03,0.378]	micro-Siemens (μS)	12.6
K^+ (funny current) Conductance, $g_{f,K}$	[0.03,0.378]	micro-Siemens (μS)	12.6
Ca^{+2} (L-type) Conductance, $PCaL$	[0.2,2.28]	nano Amps per nM (nA/nM)	11.4
Ca^{+2} (T-type) Conductance, $PCaT$	[0.02,0.064]	nano Amps per nM (nA/nM)	3.2
Rapid K^+ Rectifier Conductance, g_{Kr}	$[2.1637 \times 10^{-3}, 5 * 2.1637 \times 10^{-3}]$	micro-Siemens (μS)	5
Slow K^+ Rectifier Conductance, g_{Ks}	$[1.6576 \times 10^{-3}, 5 * 1.6576 \times 10^{-3}]$	micro-Siemens (μS)	5
Na^+ Conductance, g_{Na}	[0.0125,0.25]	micro-Seimens (μS)	20
NaK Pump Conductance, g_{NaK}	[0.063,0.4095]	nano-Amps (nA)	6.5
NaCa Exchanger Conductance, g_{NaCa}	[4,40]	nano-Amps (nA)	10

Table 3: Parameter values for NaK pump and NaCa exchanger current and s proportionality scalar $\min * (1 - s) + \max * s$.

Cell Type	g_{NaK} (nA)	g_{NaCa} (nA)	$s \in [0, 1]$
1 (center)	0.063	4	0
2	0.0695	6	0.25/9
3	0.08	6.7	0.65/9
4	0.095	8.9	1.2/9
5	0.125	13.5	2/9
6	0.164	17	3/9
7	0.2045	21	4/9
8	0.2871	29	6/9
9 (peripheral)	0.4095	40	1